Acta Mechanica Solida Sinica
https://doi.org/10.1007/s10338-023-00442-8

Underwater Directional Acoustic Source Based on Pentamode Material

Binghao Zhao[1] · Peng Wang[2] · Dongwei Wang[1] · Gengkai Hu[1]

Received: 14 July 2023 / Revised: 17 October 2023 / Accepted: 17 October 2023

Abstract
An underwater directional acoustic emitter is conceived with a highly anisotropic lattice material, whose acoustic characteristics manifest strong dependence on the orientation of the lattice material's principal axis. Exploiting these features, a cylindrical structure made of such anisotropic lattice material is engineered to possess distinct impedance values in different directions, thereby facilitating wave emission along the principal axis while inducing reflection in other directions. Notably, through numerical simulations, it is demonstrated that the emission direction can be effectively manipulated by adjusting the principal axis orientation, concurrently enhancing the emitted power. In contrast to previous directional acoustic structures, the compact emitter presented in this study can get rid of the size-wavelength constraint, enabling effective control of low-frequency waves.

Keywords Underwater · Directional emission · Pentamode material · Broadband frequency

1 Introduction

Directional acoustic emitters are able to launch beam waves in desired directions, which may concentrate wave power and extend detection distances [1]. These emitters have been found diverse applications in underwater communication, sonar systems, biomedicine, and various other domains [2–13]. Within the realm of natural biosonar systems, remarkable adaptations have evolved over millions of years [14, 15]. For instance, porpoises have developed a multiphase forehead complex, enabling the emission of directional beams crucial for communication and underwater foraging [4, 16]. This mechanism involves the utilization of air sacs positioned behind the forehead, which serve to reflect sound waves to the opposite direction, thereby it can shape the emitted beam. Inspired by this biological structure, Dong et al. [17] constructed a man-made hybrid metamaterial system consisting of multiple composite structures. This system successfully emulates the directed emission of sound beams by capitalizing on the interplay among various organs. By incorporating a reflective material as a backing and employing phase modulation structures, the system achieved significant enhancements in directivity and main lobe energy across a wide frequency range. Numerical simulations and experimental validation provide evidence that the system enables precise transmission of sound waves, resulting in a substantial amplification of acoustic energy in the desired direction. However, the proposed meta-structure predominantly operates in the high-frequency range of 40–60 kHz, and the wave propagation distance is limited due to substantial transmission loss in water.

Existing underwater directional transducers, made of conventional materials, operates effectively only when the wavelength is considerably smaller than their size [12, 16]. It is a great challenge to design low-frequency underwater directional transducers. Some efforts have been made to utilize air cavity, such as rubber air bags, as broadband wave reflectors. However, the poor resistance to pressure of air cavities induces inflation-related issues in practical applications. To address these limitations, researchers have turned their attention toward acoustic metamaterials in their pursuit of achieving low-frequency sound reflection. Chen et al. [18] conducted an investigation on a low-frequency reflective metasurface, utilizing resonators to focus acoustic wave by controlling the phase of the reflected wave. Nonetheless, the resonant mechanism limits the functionality to only a single frequency. Wu et al. [19] designed a wideband reflective

✉ Dongwei Wang
dwfwang@163.com

[1] School of Aerospace Engineering, Beijing Institute of Technology, Beijing 100081, China

[2] Wuhan Second Ship Design and Research Institute, Wuhan 430205, China

Published online: 28 November 2023

metasurface to focus underwater ultrasonic waves, employing concentric grooves with varying depths. Notably, the mechanism of the micro-grooves usually works well only at high frequencies. Recently, Chen et al. [20] and Wang et al. [21] designed low-impedance anisotropic metamaterials specifically to insulate low-frequency underwater waves. These metamaterials are composed of highly anisotropic lattices, effectively reflecting low-frequency underwater waves at specific angles between the material's principal axis and the wave direction. Inspired by the properties of these metamaterials, we design a directional underwater wave emitter, which circumvents the issues of low frequency and pressure resistance.

This paper investigates a cylindrical directional emitter for underwater acoustic waves. The mechanism and efficiency of this emitter is demonstrated through theoretical analysis and numerical simulations. The paper is arranged as follows, In Sect. 2, we investigate the sound transmission properties of an anisotropic plate and derives the necessary conditions for high reflection. In Sect. 3, a novel underwater directional emitter in the form of a thin-wall cylindrical shell is proposed using pentamode material (PM) [22]. Numerical simulations are conducted to validate the directional emissive functionality and the microstructure design. The results confirm that the emitter can effectively concentrate and amplify radiated waves in specific directions. Section 4 presents the conclusions drawn from the study.

2 Theoretical Sound Transmission Model of Anisotropic Plates

Impedance mismatching stands out as the most viable approach for achieving broadband low-frequency sound reflection. In contrast to conventional isotropic materials, the impedance of anisotropic materials is contingent upon various factors, including the rotation angle (θ_{m}) of the material principal axis relative to the normal of the interface (between the anisotropic material and its surrounding), the quasi-transverse wave velocity, material anisotropy, in addition to the density and quasi-longitudinal wave velocity. For the scenario involving normal incidence on a general orthotropic solid, its impedance can be derived as follows [19]:

$$Z = \eta \rho_{\mathrm{s}} c_{\mathrm{qL}}, \ \eta = \frac{1 + m_{\mathrm{qL}}^2}{1 + \left(c_{\mathrm{qL}}/c_{\mathrm{qT}}\right) m_{\mathrm{qL}}^2} \tag{1}$$

where ρ_{s} represents the mass density of the material, while the subscripts qL and qT refer to as the quasi-longitudinal and quasi-transverse waves, respectively. m is the parameter of polarization and will be discussed below. c denotes the wave velocity. The reflection ratio of normally incident waves at the interface between the solid and the fluid, characterized by the impedance Z_0, is quantified by $R = |Z - Z_0|/|Z + Z_0|$. This signifies that a large acoustic impedance results in a high acoustic reflection. Notably, in comparison with an isotropic solid ($Z = \rho c$), an additional parameter η appears for the anisotropic material, which allows for further adjustment of its impedance. As a result, a highly anisotropic material ($m_{\mathrm{qL}} \neq 0$, $c_{\mathrm{qL}} >> c_{\mathrm{qT}}$) with misaligned principal axes ($\theta_{\mathrm{m}} \neq 0°$ or 90°) could manifest an extremely low impedance [20]. A recent study by Chen et al. [20] has demonstrated that bimode materials or two-dimensional PMs have the capability to achieve such small impedance while currently supporting considerable pressure loads. In order to comprehensively elucidate the mechanism of sound insulation by anisotropic materials, we will in the following detail a theoretical model, where a finite size plate of the anisotropic material is considered contrary to the previous study on a semi-infinite medium [20].

Figure 1 depicts a two-dimensional underwater sound transmission model of an orthotropic plate with a general orientation θ_{m} of the material principal axis. In this model, a planar wave is normally incident onto the plate, characterized by its thickness (d) and mass density (ρ_{s}). Consequently, both reflected and transmitted waves are generated in the surrounding water medium (with mass density $\rho_0 = 1000$ kg/m^3, wave velocity $c_0 = 1500$ m/s, impedance $Z_0 = \rho_0 c_0$, and bulk modulus $K_0 = 2.25$ GPa). The expressions for the waves in the incident and transmitted regions are expressed as follows:

$$p_{\mathrm{In}} = p_{\mathrm{i}} \mathrm{e}^{ik_0 x} + p_{\mathrm{r}} \mathrm{e}^{-ik_0 x}, \quad p_{\mathrm{Tr}} = p_{\mathrm{t}} \mathrm{e}^{ik_0 x} \tag{2}$$

where p_{i}, p_{r} and p_{t} denote the amplitudes of the incident, reflected and transmitted waves, respectively. k_0 is the wavenumber in water. The time harmonic term $\mathrm{e}^{-i\omega t}$ is omitted, where ω signifies the circular frequency. For the anisotropic plate with a rotation angle θ_{m}, a normally incident plane wave excites purely longitudinal wave when the material's principal axis aligns with the interface, i.e., $\theta_{\mathrm{m}} = 0°$ or 90°. Conversely, for the angles $\theta_{\mathrm{m}} \neq 0°$ and 90°, both qL and qT waves will be excited. The wave vectors of these waves, excited by normally incident wave, align with the x axis, and the corresponding displacement fields are expressed in the form of $\boldsymbol{u}_{(\mathrm{qL,qT})} = \boldsymbol{u_0}_{(\mathrm{qL,qT})} \cdot \exp\left[ik_{(\mathrm{qL,qT})}x\right]$.

The two-dimensional constitutive law for anisotropic material in a global coordinate xOy reads,

$$\begin{pmatrix} \sigma_x \\ \sigma_y \\ \sigma_{xy} \end{pmatrix} = \begin{pmatrix} C_{11} & C_{12} & C_{16} \\ C_{12} & C_{22} & C_{26} \\ C_{16} & C_{26} & C_{66} \end{pmatrix} \begin{pmatrix} \varepsilon_x \\ \varepsilon_y \\ \varepsilon_{xy} \end{pmatrix} \tag{3}$$

where σ_x, σ_y and σ_{xy} are the stress and ε_x, ε_y and γ_{xy} are the engineering strain, respectively. The elastic matrix $\boldsymbol{C}$ for

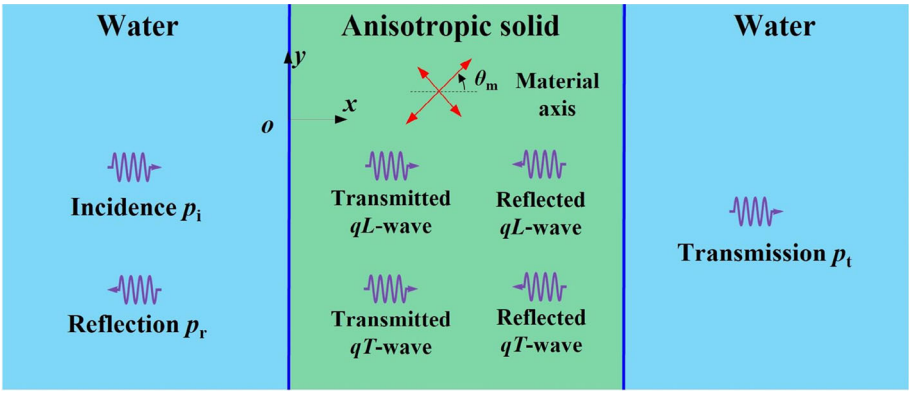

Fig. 1 Sketch of underwater acoustic transmission through an anisotropic plate

the anisotropic material with the rotation angle θ_m can be represented as $\boldsymbol{C} = \boldsymbol{N}\boldsymbol{C_0}\boldsymbol{N}$, where $\boldsymbol{C_0}$ signifies the elastic matrix in principal coordinates, and $\boldsymbol{N}$ denotes the coordinate transformation matrix [23].

$$\boldsymbol{C}_0 = \begin{pmatrix} C_{11}^0 & C_{12}^0 & 0 \\ C_{12}^0 & C_{22}^0 & 0 \\ 0 & 0 & C_{66}^0 \end{pmatrix}$$

$$\boldsymbol{N} = \begin{bmatrix} \cos^2\theta_m & \sin^2\theta_m & \sin 2\theta_m \\ \sin^2\theta_m & \cos^2\theta_m & -\sin 2\theta_m \\ -\sin\theta_m\cos\theta_m & \sin\theta_m\cos\theta_m & \cos^2\theta_m - \sin^2\theta_m \end{bmatrix} \tag{4}$$

By substituting the displacement fields into the dynamic elasticity equation $-\omega^2\rho_s\boldsymbol{u} = \nabla\cdot\boldsymbol{\sigma}$, where $\boldsymbol{\sigma} = [\sigma_{xx}, \sigma_{xy};\sigma_{xy}, \sigma_{yy}]$ is the stress tensor, the displacement fields for the qL and qT waves are, respectively, derived as

$$\begin{aligned} &\boldsymbol{u}_{qL} = \{1, m_{qL}\}^T e^{ik_{qL}x}, \quad \boldsymbol{u}_{qT} = \{1, m_{qT}\}^T e^{ik_{qT}x} \\ &m_{qL} = \tan^{-1}\frac{2C_{16}}{C_{11} - C_{66} + \sqrt{\Delta}} \\ &m_{qT} = \tan^{-1}\frac{2C_{16}}{C_{11} - C_{66} - \sqrt{\Delta}} \\ &k_{qL} = \omega\sqrt{\frac{2\rho_s}{C_{11}^0 + C_{66}^0 + \sqrt{\Delta}}}, \quad k_{qT} = \omega\sqrt{\frac{2\rho_s}{C_{11}^0 + C_{66}^0 - \sqrt{\Delta}}} \end{aligned} \tag{5}$$

where m_{qL} and m_{qT} are the parameters of polarization, k_{qL} and k_{qT} represent the wavenumbers, and $\Delta = 4(C_{16})^2 + (C_{11} - C_{66})^2$.

Considering the wave polarization, the displacement $\boldsymbol{u}$= $\{u, v\}$ in the solid can be expressed as the summation of the positive and negative-traveling qL and qT waves, given by

$$\begin{aligned} u &= t_{qT}e^{ik_{qT}x} + r_{qT}e^{-ik_{qT}x} + t_{qL}e^{ik_{qL}x} + r_{qL}e^{-ik_{qL}x} \\ v &= m_{qT}\left(t_{qT}e^{ik_{qT}x} + r_{qT}e^{-ik_{qT}x}\right) + m_{qL}\left(t_{qL}e^{ik_{qL}x} + r_{qL}e^{-ik_{qL}x}\right) \end{aligned} \tag{6}$$

where the parameters t and r denote the amplitudes of the positive- and negative-traveling waves, respectively.

The boundary conditions at the fluid–solid interfaces (at $x = 0$ and $x = d$) are derived as

$$\begin{aligned} x = 0: &\quad p_i + p_r = -\sigma_{xx}, \ \sigma_{xy} = 0, \ u = \frac{1}{\omega^2\rho_s}\frac{\partial(p_i + p_r)}{\partial x} \\ x = d: &\quad p_t = -\sigma_{xx}, \quad \sigma_{xy} = 0, \ u = \frac{1}{\omega^2\rho_s}\frac{\partial p_t}{\partial x} \end{aligned} \tag{7}$$

By combining Eqs. (2)–(7), the governing equation for sound transmission is obtained,

$$\begin{pmatrix} iA & 0 & 1 & 1 & 1 & 1 \\ 0 & 0 & iD_1 & -iD_1 & iD_2 & -iD_2 \\ 1 & 0 & iB_1 & -iB_1 & iB_2 & -iB_2 \\ 0 & -iAe_0 & e_L & e_L^{-1} & e_T & e_T^{-1} \\ 0 & 0 & iD_1e_L & -iD_1e_L^{-1} & iD_2e_T & -iD_2e_T^{-1} \\ 0 & e_0 & iB_1e_L & -iB_1e_L^{-1} & iB_2e_T & -iB_2e_T^{-1} \end{pmatrix} \begin{pmatrix} p_r \\ p_t \\ t_L \\ r_L \\ t_T \\ r_T \end{pmatrix} = \begin{pmatrix} -iA \\ 0 \\ 1 \\ 0 \\ 0 \\ 0 \end{pmatrix} \tag{8}$$

The solution of the above equation gives the expressions for the reflected and transmitted waves, provided as follows:

$$\begin{aligned} \frac{p_r}{p_i} &= -\frac{i}{\delta}\Big\{2D_1D_2\left(1 - \cos k_{qL}d\cos k_{qT}d\right) \\ &\quad + \left[A^2(D_1B_2 - B_1D_2)^2 - D_1^2 - D_2^2\right]\sin k_{qL}d\sin k_{qT}d\Big\} \\ \frac{p_t}{p_i} &= -\frac{2A}{\delta}(D_1B_2 - B_1D_2)\left(D_1\sin k_{qL}d - D_2\sin k_{qT}d\right) \end{aligned} \tag{9}$$

The detailed coefficients in Eqs. (8) and (9) can be found in Appendix. The expression for the transmitted wave in Eq. (9) implies the condition of total reflection,

$$(D_1 B_2 - B_1 D_2)\left(D_1 \sin k_{\mathrm{qL}} d - D_2 \sin k_{\mathrm{qT}} d\right) = 0 \tag{10}$$

or rewritten as

$$\left(m_{\mathrm{qL}} - m_{\mathrm{qT}}\right)\left(m_{\mathrm{qL}} \frac{\rho_{\mathrm{s}} c_{\mathrm{qL}}}{\rho_0 c_0} \sin k_{\mathrm{qL}} d - m_{\mathrm{qT}} \frac{\rho_{\mathrm{s}} c_{\mathrm{qT}}}{\rho_0 c_0} \sin k_{\mathrm{qT}} d\right) = 0 \tag{11}$$

At extremely low frequencies, an approximate total reflection is realized as both $k_{\mathrm{qL}} d$ and $k_{\mathrm{qT}} d$ tend to zero. With the exception of this trivial scenario, the condition for high reflection at low frequency ($k_{\mathrm{qL}} d \approx 0$) can be simplified as (considering $m_{\mathrm{qL}} \times m_{\mathrm{qT}} = -1$)

$$\left(1 + \frac{1}{m_{\mathrm{qL}}^2}\right) \frac{\rho_{\mathrm{s}} c_{\mathrm{qT}}}{\rho_0 c_0} \sin k_{\mathrm{qT}} d \approx 0 \tag{12}$$

Therefore, a high reflection of an anisotropic plate can be realized when its transverse wave velocity is small and its anisotropy is high. This observation aligns with the characteristics found in anisotropic materials with low impedance [20]. Moreover, in addition to impedance, the acoustic performance of the finite thickness plate is affected by many other factors, such as thickness and transverse wave velocity. To address these issues, the sound reduction index (SRI $= -20\log_{10}|p_{\mathrm{t}}/p_{\mathrm{i}}|$) is computed for a sequence of PM plates (having small transverse wave velocity and high anisotropy) with an identical thickness ($d = 0.03$ m) and impedance ($Z = 0.04 Z_0$). The detailed material parameters of the PMs are listed in Table 1, including four anisotropic PMs and one isotropic PM.

The SRI for the different plates within the frequency range of 10 Hz–10 kHz is illustrated in Fig. 2. In order to validate the theoretical model, a numerical simulation of PM 2 is also included using COMSOL Multiphysics. As shown in Fig. 2, the excellent agreement between the theoretical prediction and numerical simulation validates our theoretical model. Notably, the SRI peaks and valleys exhibit a shift toward lower frequencies as c_{qT} decreases, aligning with the observations outlined in Eq. (12). This shift indicates enhanced insulation performance in the extremely low-frequency range. These trends, however, do not apply to the isotropic PM plate. Despite possessing both a small transverse wave velocity and impedance, the isotropic PM plate demonstrates inadequate performance in the low-frequency range. Hence, it becomes evident that achieving efficient insulation in a thin plate necessitates an anisotropic material characterized by both small impedance and transverse wave velocity.

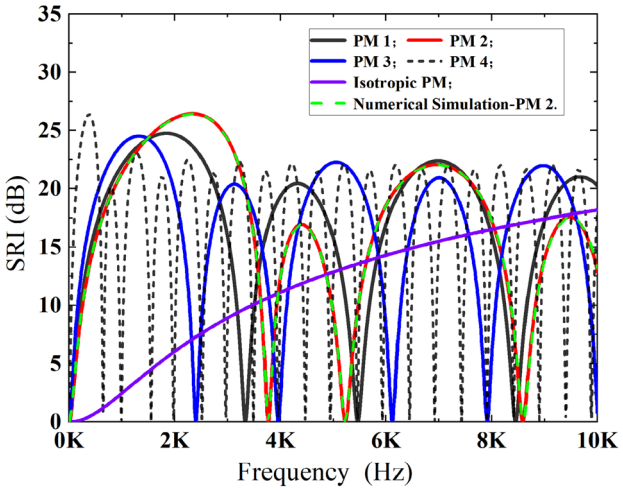

Fig. 2 SRI for anisotropic and isotropic PM plates

The superior insulation performance exhibited by the anisotropic PM plate also extends to obliquely incident cases. The SRI as a function of normalized frequency fd/c_0 and incident angle θ_{i} for the PM plates are depicted in Fig. 3. In scenarios involving oblique incident angles, the theoretical model follows a similar framework as described by Eqs. (2)–(9), but introducing an additional harmonic component $\exp(ik_y y)$ in the wave expressions in the fluid and $\exp(ik_{\mathrm{qL}y} y)$ and $\exp(ik_{\mathrm{qT}y} y)$ in the solid. The plate under consideration is composed of PM 2 from Table 1 with a thickness of $d = 0.03$ m. The contour map of SRI in Fig. 3b for $\theta_{\mathrm{m}} = 30°$ demonstrates a high reflection for various incident angles. For example, a transmission loss of 20 dB is achieved at a low frequency $f = 0.03 c_0/d$. This means that 99% of the incident wave energy is reflected by the thin plate ($d = 0.03\lambda$). It is noteworthy that this insulation behavior for general incidence angles strongly depends on the orientation of the material's principal axis. When θ_{m} is set as 0°, effective insulation is primarily observable for approximately normal incident cases, as depicted in Fig. 3c. The crosswise curves in this figure correspond to Fabry–Perot resonant transmission, due to the extremely small shear wave velocity in the plate [20]. Since Fabry–Perot resonance occurs at frequencies beyond the region of interest, these curves do not present in Fig. 3b.

3 Underwater Directional Emitter Based on PM Plate

An anisotropic PM, characterized by low impedance and low transverse wave velocity, has been identified as a viable candidate for the construction of highly reflective thin plates for underwater sound applications. Based on this property, a directional transmission emitter is proposed in the form of a thin-walled cylindrical shell composed of anisotropic PMs,

Table 1 Material parameters of the PMs

	C_{11}^0/K_0	C_{22}^0/K_0	C_{12}^0/K_0	C_{66}^0/K_0	ρ_s/ρ_0	θ_m	c_{qT}/c_0
PM 1	0.035	3.22	0.33	0.02	0.2255	28°	0.1068
PM 2	0.041	1.718	0.264	0.006	0.179	9°	0.1089
PM 3	0.0534	3.2807	0.4095	0.0298	0.321	17°	0.0759
PM 4	0.1	10	0.999	0.001	1	38.5°	0.0198
PM Iso	0.0718	0.0718	0.0718	7×10^{-6}	0.0224	–	0.0252

as illustrated in Fig. 4a. The material of this shell maintains a consistent orientation angle of its principal axis in the global Cartesian coordinate system, resulting in varying rotation angles between the normal of the local interface and the material's principal axis (see for example Points A and B in Fig. 4a). The local acoustic transmission of the shell is determined by its local material's orientation. To validate this concept, an approximately ideal pentamode material, PM 4 listed in Table 1, with a global orientation angle of 60° is selected. The impedance of PM 4 remains remarkably low over a broad range of θ_m, with the exception of angles close to 0° and 90°, as shown in Fig. 4b. Despite the analogous impedance mismatches witnessed at $\theta_m = 0°$ and 90°, the insulation performances of the plate are different. This can be explained by the transmission coefficient, represented by the left side of Eq. (11). As illustrated in Fig. 4b, the coefficient values are near zero for most material principal angles. The value around $\theta_m = 0°$ (4.6) is considerably lower than that at $\theta_m = 90°$ (184), indicating that the predominant wave transmission through the shell occurs in the direction of $\theta_m = 90°$. To illustrate this idea, we consider a shell with an inner radius of $r_1 = 0.5$ m and outer radius of $r_2 = 0.53$ m. The shell is composed of PM 4 with an orientation angle of 60° (the material's principal axis with respect to the global coordinate system) and emerged in water. A point sound source with a pressure of 1 Pa is positioned at the center of the shell.

Numerical simulations using COMSOL Multiphysics are conducted to demonstrate the directional emission characteristics of the proposed structure. For comparison, a point source configuration without the presence of the shell is

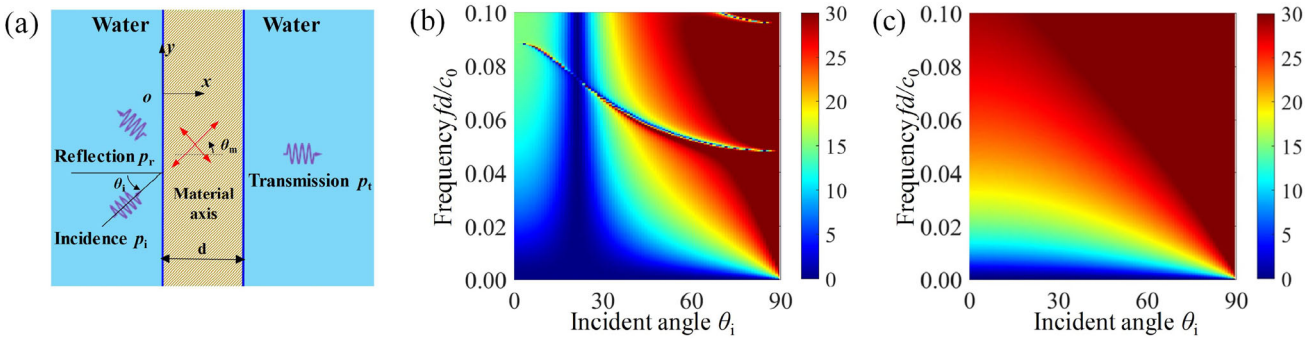

Fig. 3 **a** Sketch of underwater acoustic transmission through anisotropic plate with an obliquely incident angle θ_i. The contour map of the SRI as a function of the normalized frequency fd/c_0 and the incident angle θ_i for the PM plates with **b** $\theta_m = 30°$ and **c** $\theta_m = 0°$

Fig. 4 **a** Sketch of the emitter with a point source at center enclosed by a shell made of anisotropic PM. **b** The relative impedance of PM 4 as a function of the principal direction θ_m

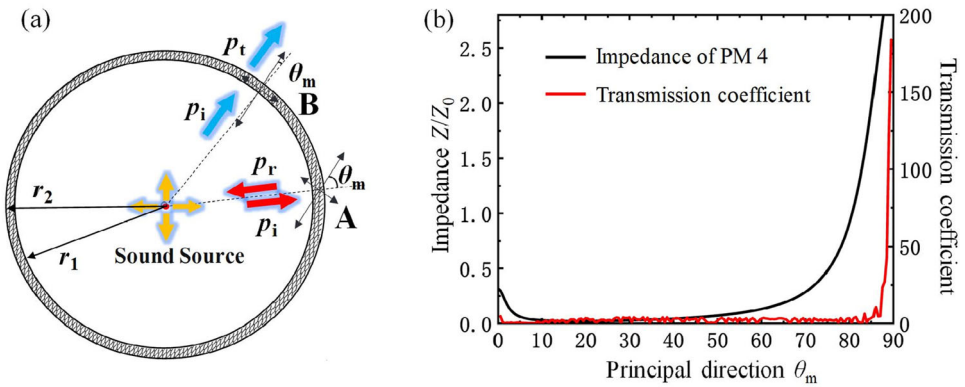

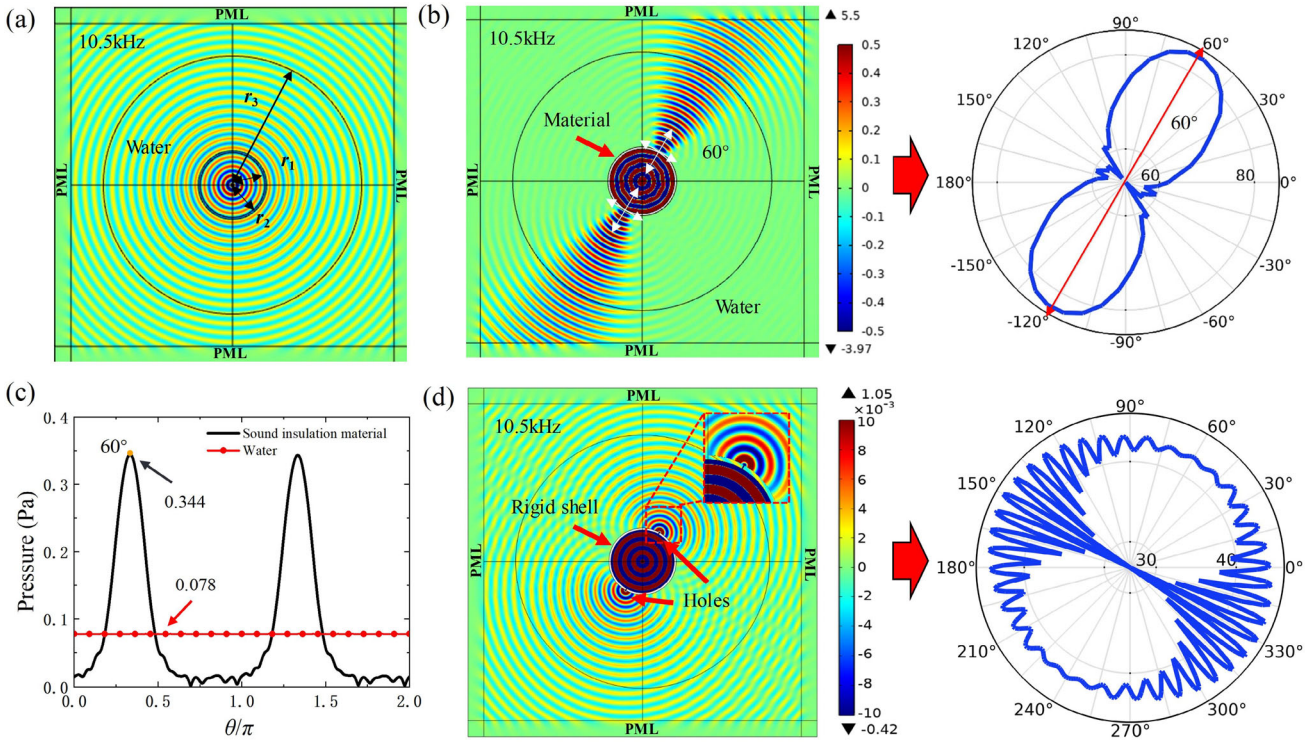

Fig. 5 Simulation results of **a** a point source, **b** an emission radiation, **c** the corresponding directivity pattern, and **d** the external radiated pressure amplitudes. **e** Simulation results and **f** the directivity pattern of an ideal acoustic rigid shell equipped with holes for comparison

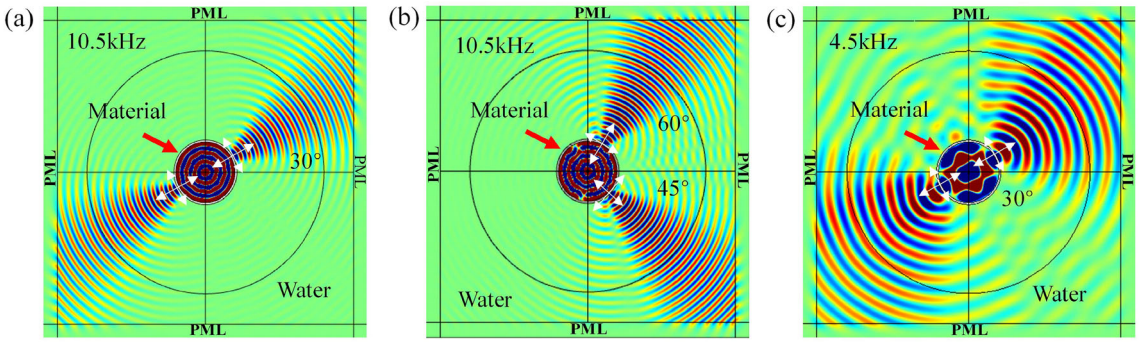

Fig. 6 Simulation results of PM with a constantly orientation angle of 30° (**a**), different orientation angles of 60° and − 45° for two halves (**b**), and emission at lower frequency of 4.5 kHz (**c**)

also included (Fig. 5a). The simulation results of the emitter notably exhibit directional transmission along the angle of 60°, as well as its opposite direction at 240° (Fig. 5b), as designed. To quantify sound directivity, sound pressures at various points on a circular path with a radius of $r_3 = 2$ m are extracted. Evidently, two peaks of pressure amplitude occur in the emissive directions (Fig. 5d), reaching a value of 0.344 Pa, which is approximately 3.4 times higher than that obtained in the absence of the shell (0.078 Pa). This enhancement is attributed to the fact that the waves in most directions are reflected by the shell and ultimately released along the emissive directions. The directivity pattern depicted in Fig. 5c serves to confirm the directional properties of this emitter.

Crucially, the operational mechanism of the emitter proposed in this paper differs from that of an ideal acoustic rigid shell equipped with transmitted holes, which is simulated and illustrated in Fig. 5e. The central angle of the holes on the cylindrical shell is 1°, resulting in an approximate width of 8 mm. Wave diffraction at holes leads to an omnidirectional radiation of waves, as shown in Fig. 5f. In contrast, the anisotropic material with principal axes aligned to the interface manifests distinct insulation characteristics for waves incident at varying angles. In other words, waves with limited incident angles can transmit through the shell, and the

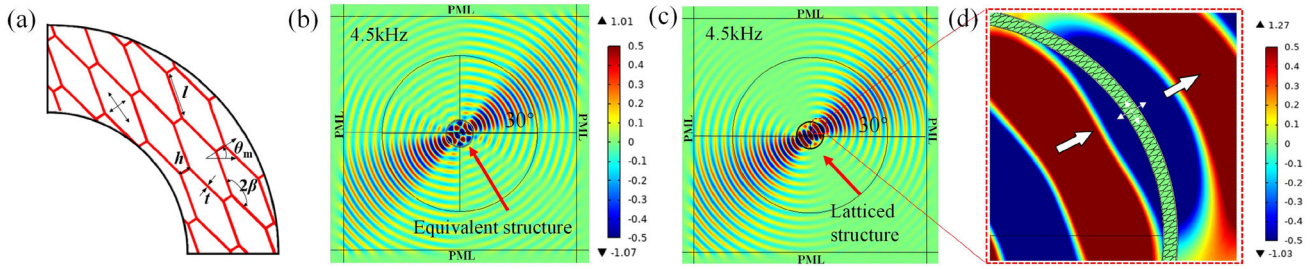

Fig. 7 **a** Local sketch of a practical PM composed of honeycomb lattices. The simulation results of the **b** equivalent and **c** practical latticed emitter at 4.5 kHz. **d** A locally enlarged drawing of the latticed shell

range of permissible incident angle shrunk as the frequency rises (Fig. 3c). Consequently, the angles of transmitted waves are confined to a narrow spectrum, which augments the emitter's directivity.

By tuning the orientation angle of the principal axis, such as setting it to 30°, the emissive direction of the shell can be adjusted accordingly, as illustrated in Fig. 6a. Additionally, the shell can be divided into two halves with different emitted angles: the top semicircular shell maintains an orientation angle of 60°, while the bottom one assumes an angle of − 45°. Simulation results demonstrate the presence of two emissive directions along these two material principal axes (Fig. 6b). This design flexibility allows for the realization of various directional emission requirements. For the purpose of showcasing the directional emission with clarity, a wave frequency of 10.5 kHz is selected for the sound source. Interestingly, as depicted in Fig. 6c, the emissive property remains unchanged even as the frequency decreases to 4.5 kHz. This confirms the broadband nature of the proposed emitter. Notably, as the frequency decreases, the scattering angle of the radiated wave beam increases. This can be explained by the widening scope of the angle of the transmitted wave corresponding to the frequency decrease, as shown in Fig. 3c.

In the previous simulations, the shells are designed with homogeneous PMs. In order to actualize the proposed emitter, it is essential to identify the corresponding microstructure. It has been established that a honeycomb lattice can approximate a PM structure when the beams are sufficiently thin [24]. In this section, the desired anisotropic PM for the emitter is realized using a honeycomb lattice composed of

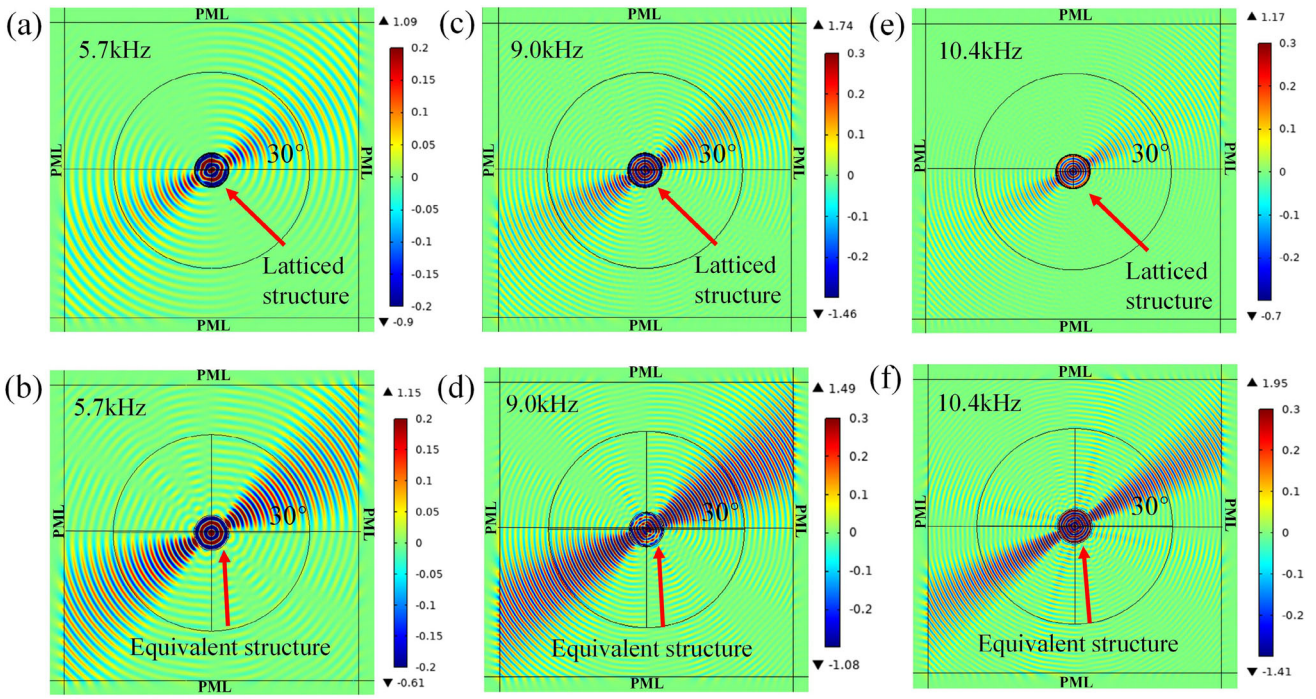

Fig. 8 Simulation results of latticed and equivalent directional emission structures at frequencies of **a**, **b** 5.7 kHz, **c**, **d** 9.0 kHz and **e**, **f** 10.4 kHz, respectively

Aluminum (with material parameters: mass density $\rho_{\mathrm{Al}} = 2700\ \mathrm{kg/m_3}$, Young's modulus $E_{\mathrm{Al}} = 69$ GPa and Poisson's ratio $v_{\mathrm{Al}} = 0.33$). The lattice cell is characterized by three dimensionless parameters: the length ratio h/l, the dimensionless beam thickness t/l and the topology angle β (Fig. 7a). Considering the machinability of the lattice, the PM 2 in Table 1 with practical parameters, instead of ideal PM 4, is chosen to construct the structure. To conduct the investigation, a particular lattice cell with $\beta = 74°$, $h/l = 0.25$, $t/l = 0.03$ and an orientation angle of 30° is employed to homogenize the elastic matrix and mass density of PM 2. Subsequently, the unit cells of the lattice are arranged periodically to form a shell with a thickness of 0.03 m, sealed at the interfaces by aluminum cylindrical thin borders. To verify the lattice structure, a simulation of a homogenous PM shell with equivalent parameters and thin borders is also conducted (Fig. 7b). The simulation results of the lattice structure agree with those of the equivalent shell, demonstrating direction emissions from the practical emitter.

It is important to highlight that the homogenization process employed for the honeycomb lattice is conducted in a static manner, resulting in the inherent behavior of PM within a broadband frequency range. The reliability of the homogenization method is confirmed through emission simulations conducted at different frequencies. Figure 8a–f shows the results of both the equivalent and latticed emitters at frequencies of 5.7 kHz, 9.0 kHz and 10.4 kHz, respectively. These results demonstrate that the directional emission can be achieved within a broadband frequency range.

4 Conclusion

In this study, the sound insulation properties of thin plates composed of anisotropic material are investigated. The use of pentamode materials is proposed to achieve broadband low-frequency insulation. Building upon these materials, an underwater emitter capable of directional emission is designed. The emitter exhibits a significant design flexibility, allowing for the control of emissive directions. Numerical simulations are conducted to validate the efficacy and broadband nature of the structures with practical lattice microstructures. The simulations reveal that the waves inside the emitter are concentrated along the desired emissive direction, resulting in enhanced power emission in those specific directions.

Acknowledgements This work was supported by the National Natural Science Foundation of China (Grants No. 11991030, No. 11991033, No. 12202054, and No. 11802017).

Appendix: Coefficients in the governing equation and the expressions of the waves

The coefficients in Eqs. (8) and (9) are listed as follows

$$
\begin{aligned}
A &= k_0/\rho_0\omega^2 \\
B_1 &= C_{11}k_{\mathrm{qL}} + m_{\mathrm{qL}}C_{16}k_{\mathrm{qL}} = \omega\rho_{\mathrm{s}}c_{\mathrm{qL}} \\
B_2 &= C_{11}k_{\mathrm{qT}} + m_{\mathrm{qT}}C_{16}k_{\mathrm{qT}} = \omega\rho_{\mathrm{s}}c_{\mathrm{qT}} \\
D_1 &= C_{16}k_{\mathrm{qL}} + m_{\mathrm{qL}}C_{66}k_{\mathrm{qL}} = m_{\mathrm{qL}}B_1 \\
D_2 &= C_{16}k_{\mathrm{qT}} + m_{\mathrm{qT}}C_{66}k_{\mathrm{qT}} = m_{\mathrm{qT}}B_2 \\
\mathrm{e_L} &= \mathrm{e}^{idk_{\mathrm{qL}}},\quad e_{\mathrm{L}}^{-1} = \mathrm{e}^{-idk_{\mathrm{qL}}},\quad \mathrm{e_T} = \mathrm{e}^{idk_{\mathrm{qT}}} \\
\mathrm{e}_{\mathrm{T}}^{-1} &= \mathrm{e}^{-idk_{\mathrm{qT}}},\quad e_0 = \mathrm{e}^{idk_0} \\
\delta &= \Big\{ -2iD_1D_2\big(1-\cos k_{\mathrm{qT}}d\cos k_{\mathrm{qL}}d\big) \\
&\quad + i\Big[D_1^2 + D_2^2 + A^2(D_1B_2 - B_1D_2)^2\Big]\sin k_{\mathrm{qT}}d\sin k_{\mathrm{qL}}d\Big\} \\
&\quad + 2A(D_1B_2 - B_1D_2) \\
&\quad \big(D_2\sin k_{\mathrm{qT}}d\cos k_{\mathrm{qL}}d - D_1\cos k_{\mathrm{qT}}d\sin k_{\mathrm{qL}}d\big)
\end{aligned}
\tag{A1}
$$

The amplitudes of the waves are then expressed as

$$
\begin{aligned}
t_{\mathrm{qL}} &= \frac{-AD_2}{\delta}(D_1 - \mathrm{e}^{-ik_{\mathrm{qL}}d}(D_1\cos k_{\mathrm{qT}}d \\
&\quad + i(D_2 - AD_1B_2 + AB_1D_2)\sin k_{\mathrm{qT}}d)) \\
r_{\mathrm{qL}} &= \frac{-AD_2}{\delta}(D_1 - \mathrm{e}^{ik_{\mathrm{qL}}d}(D_1\cos k_{\mathrm{qT}}d - i(D_2 \\
&\quad + AD_1B_2 - AB_1D_2)\sin k_{\mathrm{qT}}d)) \\
t_{\mathrm{qT}} &= \frac{-AD_1}{\delta}(D_2 - \mathrm{e}^{-ik_{\mathrm{qT}}d}(D_2\cos k_{\mathrm{qL}}d + i(D_1 \\
&\quad + AD_1B_2 - AB_1D_2)\sin k_{\mathrm{qL}}d)) \\
r_{\mathrm{qT}} &= \frac{-AD_1}{\delta}(D_2 - \mathrm{e}^{ik_{\mathrm{qT}}d}(D_2\cos k_{\mathrm{qL}}d - i(D_1 - AD_1B_2 \\
&\quad + AB_1D_2)\sin k_{\mathrm{qL}}d))
\end{aligned}
\tag{A2}
$$

References

1. Håkansson A, Torrent D, Cervera F, Sánchez-Dehesa J. Directional acoustic source by scattering acoustical elements. Appl Phys Lett. 2007;90(22): 224107.
2. Butler SC. Properties of transducers: Underwater sound sources and receivers. Naval Undersea Warfare Center Division Newport United States. 2018.

3. Chen Z, Yan B, Zhang X. Propagation characteristics of underwater plasma pulse sound source. In: Journal of Physics: Conference Series. IOP Publishing Ltd; 2019. vol. 1237(2). p. 022088
4. Cheong YJ, Lee WJ, Ruesch A, Schalles M, Kainerstorfer J, Shinn-Cunningham B. Modeling and interpreting the head-related transfer function to understand directional hearing in bottlenose dolphins. J Acoust Soc Am. 2023; 153(3_supplement): A187-A187.
5. Paolo C, Milena M, Paolo C. Acoustic beamforming for noise source localization – Reviews, methodology and applications. Mech Syst Signal Pr. 2019;120:422–48.
6. Dzsotjan D, Kastel J, Fleischhauer M. Dipole-dipole shift of quantum emitters coupled to surface plasmons of a nano-wire. Phys Rev B. 2011;84(7): 075419.
7. Guan Z, Liu L, Xu X, Liu A, Wu H, Li J, Yang WO. A self-powered acoustic sensor excited by ultrasonic wave for detecting and locating underwater ultrasonic sources. Nano Energy. 2022;104: 107879.
8. Hu J, Hong L, Yin L, Lan Y, Sun H, Guo R. Research and fabrication of broadband ring flextensional underwater transducer. Sensors-Basel. 2021;21(4):1548.
9. Huang Q, Wang H, Hao S, Zhong C, Wang L. Design and fabrication of a high-frequency single-directional planar underwater ultrasound transducer. Sensors-Basel. 2019;19(19):4336.
10. Christensen J, de Abajo FJG. Anisotropic metamaterials for full control of acoustic waves. Phys Rev Lett. 2012;108(12): 124301.
11. Qiao G, Liu QP, Liu SZ, Muhammad B, Wen MH. Symmetric connectivity of underwater acoustic sensor networks based on multimodal directional transducer. Sensors-Basel. 2021;21(19):6548.
12. Sineiro GD. Underwater multimode directional transducer evaluation. Monterey, California. Naval Postgraduate School. 2003.
13. Li X, Xie H, Kang Y, Wu X. A brief review and prospect of experimental solid mechanics in China. Acta Mech Solida Sin. 2010;23(6):498–548.
14. Zhuang Q, Müller R. Numerical study of the effect of the noseleaf on biosonar beamforming in a horseshoe bat. Phys Rev E. 2007;76(5): 051902.
15. Zhang Y, Song Z, Wang X, Cao W, Au WW. Directional acoustic wave manipulation by a porpoise via multiphase forehead structure. Phys Rev Appl. 2017;8(6): 064002.
16. Zhang Y, Gao X, Zhang S, Cao W, Tang L, Wang D, Li Y. A biomimetic projector with high subwavelength directivity based on dolphin biosonar. Appl Phys Lett. 2014;105(12): 123502.
17. Dong E, Zhang Y, Song Z, Zhang T, Cai C, Fang NX. Physical modeling and validation of porpoises'directional emission via hybrid metamaterials. Natl Sci Rev. 2019;6(5):921–8.
18. Chen Z, Yan F, Negahban M, Li Z. Resonator-based reflective metasurface for low-frequency underwater acoustic waves. J Appl Phys. 2020;128(5): 055305.
19. Wu X, Xia X, Tian J, Liu Z, Wen W. Broadband reflective metasurface for focusing underwater ultrasonic waves with linearly tunable focal length. Appl Phys Lett. 2016;108(16): 163502.
20. Chen Y, Zhao B, Liu X, Hu G. Highly anisotropic hexagonal lattice material for low frequency water sound insulation. Extreme Mech Lett. 2020;40: 100916.
21. Wang Y, Zhao H, Yang H, Liu J, Yu D, Wen J. Topological design of lattice materials with application to underwater sound insulation. Mech Syst Signal Pr. 2022;171: 108911.
22. Nie X, Chen Y, Liu X. Scattering analysis and optimization of spherical acoustic cloak with unideal pentamode material. Acta Mech Solida Sin. 2019;33(3):347–60.
23. Zhao B, Wang D, Zhou P, Liu X, Hu G. Design of load-bearing materials for isolation of low-frequency waterborne sound. Phys Rev Appl. 2022;17(3): 034065.
24. Chen Y, Liu X, Hu G. Latticed pentamode acoustic cloak. Sci Rep-UK. 2015;5(1):15745.